**Astronomy
&
Astrophysics**

Combining magneto-hydrostatic constraints with Stokes profiles inversions

II. Application to Hinode/SP observations

J. M. Borrero[1], A. Pastor Yabar[2], and B. Ruiz Cobo[3,4]

[1] Leibniz-Institut für Sonnenphysik, Schöneckstr. 6, 79110, Freiburg, Germany
e-mail: borrero@leibniz-kis.de
[2] Institute for Solar Physics, Department of Astronomy, Stockholm University, AlbaNova University Centre, 10691 Stockholm, Sweden
[3] Instituto de Astrofísica de Canarias, Avd. Vía Láctea s/n, 38205 La Laguna, Spain
[4] Departamento de Astrofísica, Universidad de La Laguna, 38205, La Laguna, Tenerife, Spain

ABSTRACT

Context. Inversion techniques applied to the radiative transfer equation for polarized light are capable of inferring the physical parameters in the solar atmosphere (temperature T, magnetic field $\boldsymbol{B}$, and line-of-sight velocity v_{los}) from observations of the Stokes vector (i.e., spectropolarimetric observations) in spectral lines. Inferences are usually performed in the $(x, y, \tau_{\mathrm{c}})$ domain, where τ_{c} refers to the optical-depth scale. Generally, their determination in the (x, y, z) volume is not possible due to the lack of a reliable estimation of the gas pressure, particularly in regions of the solar surface harboring strong magnetic fields.
Aims. We aim to develop a new inversion code capable of reliably inferring the physical parameters in the (x, y, z) domain.
Methods. We combine, in a self-consistent way, an inverse solver for the radiative transfer equation (Firtez-DZ) with a solver for the magneto-hydrostatic equilibrium, which derives realistic values of the gas pressure by taking the magnetic pressure and tension into account.
Results. We test the correct behavior of the newly developed code with spectropolarimetric observations of two sunspots recorded with the spectropolarimeter (SP) instrument on board the Hinode spacecraft, and we show how the physical parameters are inferred in the (x, y, z) domain, with the Wilson depression of the sunspots arising as a natural consequence of the force balance. In particular, our approach significantly improves upon previous determinations that were based on semiempirical models.
Conclusions. Our results open the door for the possibility of calculating reliable electric currents in three dimensions, $\boldsymbol{j}(x, y, z)$, in the solar photosphere. Further consistency checks would include a comparison with other methods that have recently been proposed and which achieve similar goals.

Key words. sunspots – Sun: magnetic fields – Sun: photosphere – polarization – magnetohydrodynamics (MHD)

1. Introduction

Inversion techniques applied to the radiative transfer equation for polarized light are arguably the best tools at our disposal for inferring the physical properties (temperature T, magnetic field $\boldsymbol{B}$, and line-of-sight velocity v_{los}) of the solar atmosphere (Socas-Navarro 2001; del Toro Iniesta 2003a; Bellot Rubio et al. 2006; Ruiz Cobo et al. 2007; del Toro Iniesta & Ruiz Cobo 2016). Because the natural scale to describe how photons propagate is the so-called optical depth (τ), the physical properties are inferred in the $(x, y, \tau_{\mathrm{c}})$, where τ_{c} refers to the continuum optical depth. Here "continuum" means any wavelength where the absorption is only due to bound-free and free-free transitions (Mihalas 1970, Sect. 4.4).

In order to infer the physical parameters in the (x, y, z) domain, additional constraints must be invoked. By far, the most widely used has been hydrostatic equilibrium. However, this assumption is adequate only in regions where the magnetic field is force-free (i.e., Lorentz force $\propto \boldsymbol{j} \times \boldsymbol{B} = 0$) and the plasma is stationary (i.e., no time dependence) and static (i.e., no velocities). In many regions of the solar atmosphere,

notably in sunspots, the force-free assumption breaks down and a different method must therefore be employed.

The first authors that attempted a more realistic treatment were Martinez Pillet & Vazquez (1990, 1993), Solanki et al. (1993). They all employed the theoretical model from Maltby (1977), which considers an axially symmetric magnetic field around the sunspot in order to account for the magnetic pressure and tension. This approach had been used until recently (see e.g., Mathew et al. 2004), until the pioneering work of (Puschmann et al. 2010, hereafter referred to as PUS2010), who presented a new method based on the minimization of the Lorentz force and $\boldsymbol{\nabla} \cdot \boldsymbol{B}$ in order to transform the physical parameters from the $(x, y, \tau_{\mathrm{c}})$ domain into the (x, y, z) domain. Despite its importance, PUS2010 suffers a couple of drawbacks. The first is that the minimization, based on a genetic algorithm, is very slow due to the large number of free parameters and therefore can only deal with relatively small regions. More important, however, is the fact that the gas pressure is modified in the process of inferring the physical parameters in the (x, y, z) domain, and therefore the physical parameters are not able to provide the best possible fit to the observed polarization signals.
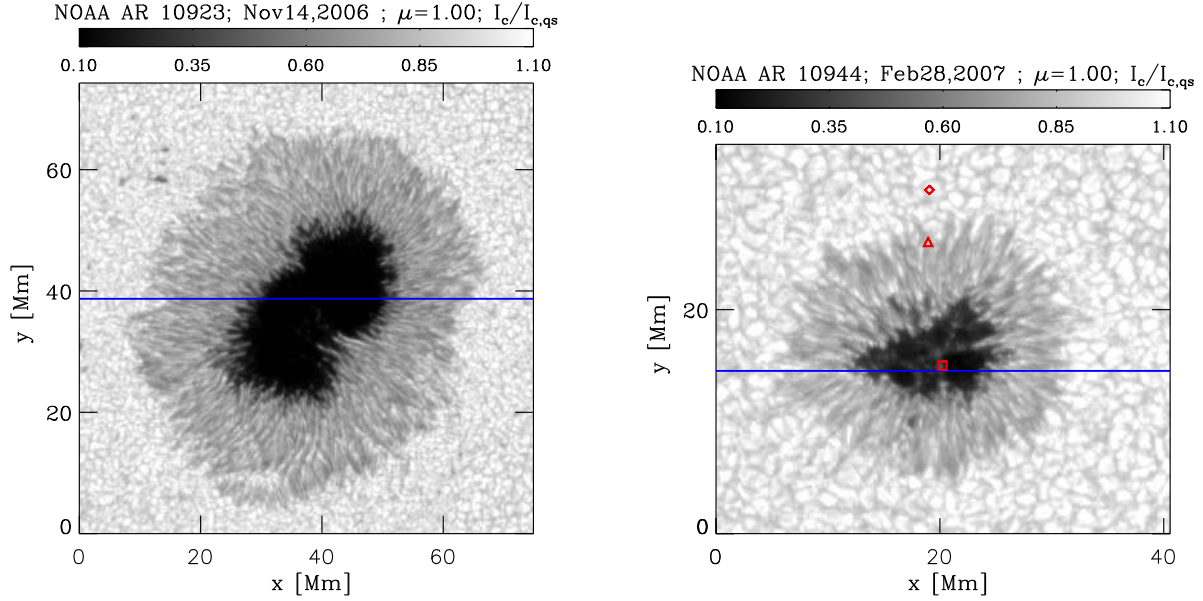
Fig. 1. Maps of the normalized continuum intensity, $I_c/I_{c,qs}$, for the two sunspots analyzed in this work. *Left*: NOAA AR 10923 observed on November 14, 2006. *Right*: NOAA AR 10944 observed on February 28, 2007. At the time of the observations, both sunspots were located at disk center. Regions marked with red symbols and solid blue lines will be studied in more detail later on.

The results from PUS2010 have sparked a new interest in developing an inversion code for the radiative transfer equation that is capable of inferring the physical parameters in the solar atmosphere in the geometrical (x, y, z) three-dimensional domain. This has resulted in a number of new approaches, beginning with adapting the PUS2010 method to minimize only $\nabla \cdot \boldsymbol{B}$ but in a much larger area (Löptien et al. 2018, 2020). Methods that rely on magneto-hydrodynamic (MHD) simulations have also been developed, with some using these simulations as training sets for artificial neural networks (Carroll & Kopf 2008) and convolutional neural networks (Asensio Ramos & Díaz Baso 2019), while others employing them as a database of physical parameters capable of fitting the observed polarization signals (Riethmüller et al. 2017).

We have developed an alternative approach that is loosely based on PUS2010. In Pastor Yabar et al. (2019), we presented an inversion code for the radiative transfer equation that works directly in the (x, y, z) domain, and we showed that the reliability of inferences in the z-scale depend upon the realism of the gas pressure (P_g). In Borrero et al. (2019), we presented a method that is based on the magneto-hydrostatic (MHS) equilibrium instead of hydrostatic equilibrium and can be used to infer very realistic values of P_g. In this article, we come full circle and demonstrate how the approaches presented in the previous two papers can be combined to determine accurate physical parameters in the solar atmosphere in the (x, y, z) domain, by applying our newly developed methods to spectropolarimetric observations with high spatial and spectral resolution.

2. Hinode/SP observations

The observations employed in this work correspond to spectropolarimetric observations (i.e., Stokes vector $\mathbb{I}^{obs}$) of two neutral iron (Fe I) spectral lines at 630 nm. The Stokes vector possesses four components, $\mathbb{I} = (I, Q, U, V)$, where I refers to the total intensity, Q and U to the linear polarization, and V to the circular polarization (see Sect. 3.3 in del Toro Iniesta 2003b).

The observations were carried out with the spectropolarimeter (SP; Lites et al. 2001; Ichimoto et al. 2007) attached to the Solar Optical Telescope (SOT; Suematsu et al. 2008; Tsuneta et al. 2008; Shimizu et al. 2008) on board the Japanese satellite Hinode (Kosugi et al. 2007). The spectral region containing the two aforementioned Fe I lines was measured across $\Lambda = 112$ wavelength points with a wavelength sampling of about 21.5 mÅ. The atomic parameters for these spectral lines can be found in Borrero et al. (2014) (see their Table 1). The SP is a slit-spectrograph where a given region is scanned spatially. For each slit position, the light is integrated for a total of 4.8 s, yielding a noise level of $\sigma = 10^{-3}$ in units of the quiet-Sun continuum intensity. The spatial sampling along the slit and perpendicular to it is about 0.16 arcsec (i.e., $dx = dy = 120$ km at disk center).

In this work, we analyze spectropolarimetric data from two different sunspots: NOAA AR 10923 and NOAA AR 10944. Both spots were observed very close to disk center $\mu \approx 1.0$, on November 14, 2006 (at around 7:15 UT) and February 28, 2007 (at around 11:50 UT), respectively. Maps of the continuum intensity I_c, normalized to the quiet-Sun continuum intensity $I_{c,qs}$, can be seen in Fig. 1 for AR 10923 (left) and AR 10944 (right). The analyzed maps possess the following horizontal dimensions (in pixels): $L = 645$, $M = 640$ and $L = 350$, $M = 300$, respectively.

3. Methodology

3.1. Stokes inversion with Firtez-DZ

The Stokes inversion code employed in this work is Firtez-DZ (Pastor Yabar et al. 2019). A graphical sketch of how Firtez-DZ operates is presented in Fig. 2 and is highlighted in red boxes. A more detailed description of this figure will be given throughout this section. Firtez-DZ needs guesses of the physical parameters C^{ij} in the solar atmosphere as inputs. We refer to these physical parameters with the super-indexes i, j, where i-even indicates that we are currently inside the Stokes inversion loop within Firtez-DZ, while i-odd implies that we are inside the MHS module. Index j stands for the iteration number within
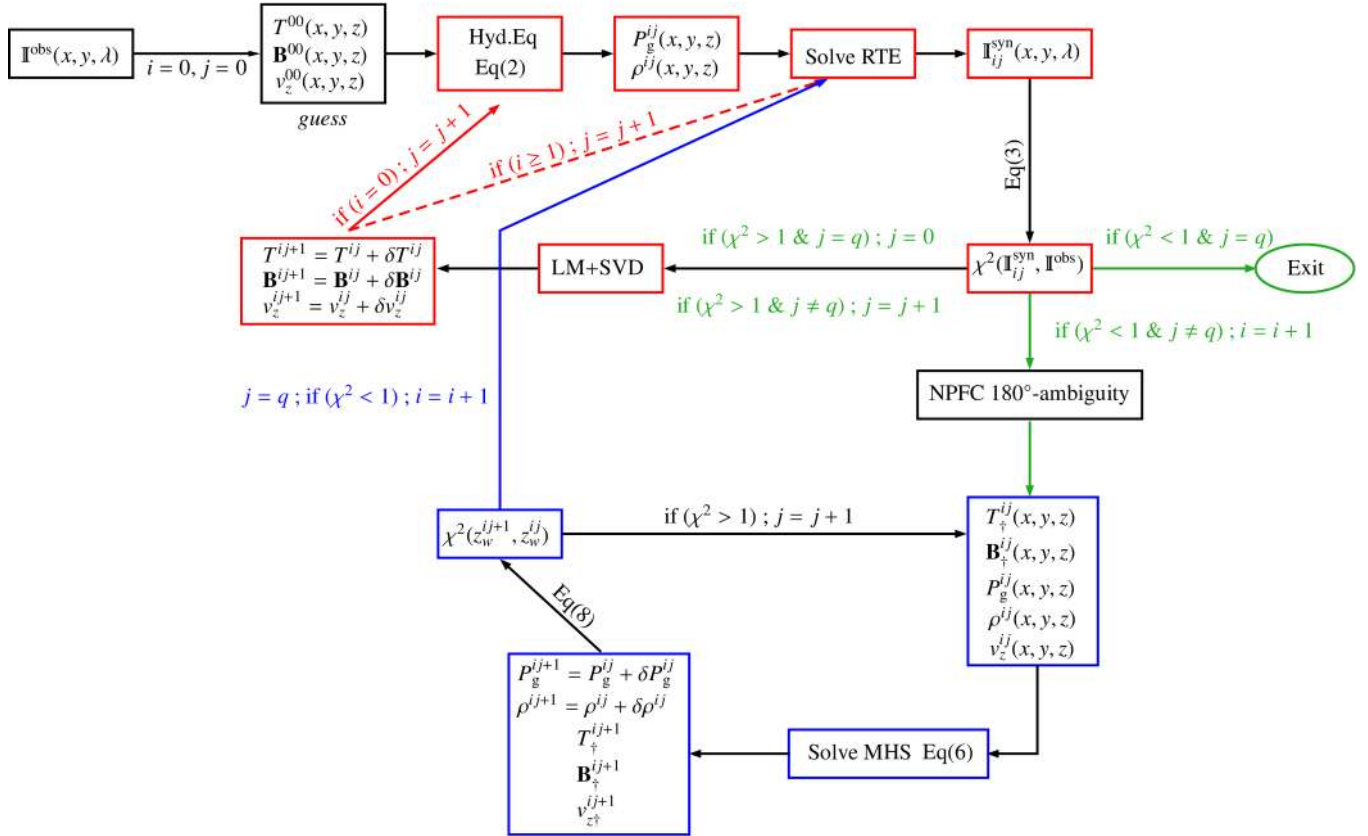
Fig. 2. Flow chart indicating the inversion process of the radiative transfer equation (RTE) for polarized light (i.e., the Stokes inversion) combined with MHS constraints. The black squares denote the acquisition of the observed Stokes vector $\mathbb{I}^{\mathrm{obs}}(x, y, \lambda)$ and the determination of an initial set of physical parameters ($T^{00}(x, y, z)$, $\mathbf{B}^{00}(x, y, z)$) with which we can start the inversion (i.e., a guess). The red squares indicate the inversion process as carried out by the Firtez-DZ code. This is described in detail in Sect. 3.1. Blue squares correspond to the steps carried out by the MHS module (see Sect. 3.3 for details). Finally, green squares and arrows indicate locations where an interplay between Firtez-DZ and the MHS module are needed in order to assess if convergence and exit conditions are achieved (see Sect. 3.4 for more information).

either Firtez-DZ or the MHS module and is reset to $j = 0$ every time the Stokes inversion and MHS modules communicate with each other.

The aforementioned physical parameters C^{ij} stand for: temperature (T^{ij}), three components of the magnetic field (B_x^{ij}, B_y^{ij}, B_z^{ij}), and the line-of-sight component of the velocity (v_{los}^{ij}), all as a function of the Cartesian[1] coordinates (x, y, z). Besides these physical parameters, Firtez-DZ needs the density ρ^{ij} and gas pressure P_{g}^{ij}. The former can be obtained from the latter if the temperature is known by using the equation of state:

$$\rho^{ij} = \frac{u}{K_{\mathrm{b}}} \frac{\mu^{ij} P_{\mathrm{g}}^{ij}}{T^{ij}}, \tag{1}$$

where u and K_{b} refer to the atomic unit mass and the Boltzmann constant, respectively: $u = 1.6605 \times 10^{-24}$ g and $K_{\mathrm{b}} = 1.3806 \times 10^{-16}$ erg K^{-1}. The mean molecular weight μ is a function of T and P_{g}, and its determination involves the iterative computation of the Saha ionization equation and the Boltzmann equation for the occupancy of the energy levels within an atom (Mihalas 1970).

The question that remains is how to determine the gas pressure P_{g}^{ij} at every j-step during the inversion process. At $i = 0$, the

MHS module has not yet been employed, so we need to rely on hydrostatic equilibrium approximation along the vertical direction:

$$\frac{\partial P_{\mathrm{g}}^{0j}}{\partial z} = -\rho^{0j} g, \tag{2}$$

where $g = 2.74$ cm s^{-2} is the Sun's gravitational acceleration. The gas pressure is recalculated at every j-step during the Stokes inversion as long as $i = 0$ (i.e., hydrostatic equilibrium). This is indicated by the solid red arrow in Fig. 2. For $i \geq 1$, the MHS module (Sect. 3.3) already provides the gas pressure, and therefore we do not need to calculate it. Indeed, for $i \geq 1$, Firtez-DZ keeps P_{g} constant during the Stokes inversion (i.e., j-step; see dashed red arrow in Fig. 2).

With all these ingredients, Firtez-DZ solves the radiative transfer equation for polarized light in the z-scale (Landi Degl'Innocenti & Landi Degl'Innocenti 1985) under the assumption of local thermodynamic equilibrium and computes the polarized spectrum (i.e., Stokes vector $\mathbb{I}_{ij}$) of atomic spectral lines in the Zeeman regime as a function of wavelength and horizontal grid position (x, y, λ). This Stokes vector is referred to as a "synthetic" Stokes vector and is denoted as $\mathbb{I}_{ij}^{\mathrm{syn}}(x, y, \lambda)$. The four components of the Stokes vector (see Sect. 2) are generically referred to as $I_{s,ij}$ ($I_{s=1} = I, I_{s=2} = Q, I_{s=3} = U, I_{s=4} = V$). The $\mathbb{I}_{ij}^{\mathrm{syn}}(x, y, \lambda)$ is then compared to the observed Stokes vector

---

[1] In this paper we will always assume that the observer's line-of-sight is parallel to the gravity direction $-z$ and therefore $v_{\mathrm{los}} = v_z$. This is possible because the selected observations are very close to disk center ($\mu \approx 1$; see Sect. 2).

Table 1. Summary of indexes employed in Sect. 3.

Index	Phys.mag	Ref.	Step size
i-even, j-any	$\chi^2(\mathbb{I}^{\text{syn}}_{ij}, \mathbb{I}^{\text{obs}})$	Sect. 3.1; Eq. (3)	na
i-odd, j-any	$\chi^2(z_w^{ij+1}, z_w^{ij})$	Sect. 3.3; Eq. (8)	na
$k = 1, \ldots, \Lambda = 112$	$\mathbb{I}$	Sect. 2	21.5 mÅ
$s = 1, \ldots, 4$	$\mathbb{I}$	Sect. 3.1	na
$l = 1, \ldots, L$	x	Sect. 2	120 km
$m = 1, \ldots, M$	y	Sect. 2	120 km
$n = 1, \ldots, N = 128$	z	Sect. 3.1	12 km

$\mathbb{I}^{\text{obs}}(x, y, \lambda)$ via a χ^2-merit function:

$$\chi^2(\mathbb{I}^{\text{syn}}_{ij}, \mathbb{I}^{\text{obs}}) = \frac{1}{4ML\Lambda - F} \sum_{l=1}^{L} \sum_{m=1}^{M} \sum_{k=1}^{\Lambda} \sum_{s=1}^{4} w_s^2 [I_s^{\text{obs}}(x_l, y_m, \lambda_k)$$
$$- I_{s,ij}^{\text{syn}}(x_l, y_m, \lambda_k)]^2 \quad \text{with } i \text{ even}, \qquad (3)$$

where the sum runs for all grid points on the horizontal plane (x, y) (indexes l and m, respectively), for all observed wavelengths (index k) and for all four Stokes parameters (index s). In order to help the reader keep track of all indexes, a summary is provided in Table 1. In Eq. (3), F stands for the total number of free parameters employed in the inversion (see Table 2). The w_s factors in Eq. (3) are used as weights during the inversion of the radiative transfer equation (see Eq. (35) del Toro Iniesta & Ruiz Cobo 2016), and χ^2 is normalized such that a value of $\chi^2 < 1$ indicates a good fit between $\mathbb{I}^{\text{obs}}$ and $\mathbb{I}^{\text{syn}}_{ij}$. In this paper, the inversion is performed such that it gives three times more weight to the linear polarization profiles Q and U than to I: $w_2 = w_3 = 3w_1$, and two times more weight to the circular polarization V than to I: $w_4 = 2w_1$. The weight given to Stokes I was taken as the inverse of the noise (see Sect. 2): $w_1 = 1/\sigma$.

Analytical derivatives of χ^2 with respect to the physical parameters[2] are calculated and fed into a Levenberg-Marquardt (LM) algorithm (Press et al. 1986) that, along with the singular decomposition value (SVD) method (Golub & Kahan 1965), provides the new physical parameters in the solar atmosphere C^{ij+1} as a function of (x, y, z); these new parameters produce a better match between the synthetic and observed Stokes profiles: $\chi^2_{ij+1} < \chi^2_{ij}$. This process continues iteratively until the best possible match between the synthetic and observed Stokes vector is found (i.e., χ^2-minimization).

We will now assume that the minimization is achieved after $j = p$ iterations of the Stokes inversion process (i-even), thus proving the physical parameters in the solar atmosphere, $[C^{ip}, P_g^{ip}, \rho^{ip}]$, as a function of (x, y, z). If $i = 0$, Firtez-DZ provides only a "first estimation" of the physical parameters in the solar atmosphere as a function of (x, y, z) because, as discussed in Pastor Yabar et al. (2019), their reliability in the (x, y, z) domain depends upon the accuracy of the gas pressure $P_g(x, y, z)$, whose inference is in turn hindered by the limitations of hydrostatic equilibrium employed at $i = 0$. In order to improve the determination of $P_g(x, y, z)$, all physical parameters (T^{ip}, P_g^{ip}, ρ^{ip}, B_x^{ip}, B_y^{ip}, B_z^{ip}, and v_z^{ip}) are then passed onto the disambiguation module (Sect. 3.2) and from there to the MHS module (Sect. 3.3).

---

[2] These derivatives are ultimately written as a function of the derivatives of the Stokes vector with respect to the physical parameters: the so-called response functions (see Sect. 6 in del Toro Iniesta & Ruiz Cobo 2016).

Table 2. Summary of free parameters in Firtez-DZ (Sect. 3.1).

C^{ij}	$i = 0$	$i = 2$	$i = 4$	$i = 6$
T	8	8	8	8
B_x	1	1	4	4
B_y	1	1	4	4
B_z	1	1	4	4
v_z	1	1	4	4

With this, we increase the i-index by one (i is now odd), and, since the MHS module has its own internal iteration that is independent from the Stokes inversion, we also reset the j-index to zero. This step is indicated by the green arrow in Fig. 2.

During the inversion process, the three-dimensional volume is discretized in L, M, and N points along each of the three Cartesian coordinates, x, y, and z, respectively. The grid sizes are denoted as dx, dy, and dz. In all our inversions, we discretized the vertical direction with $N = 128$ grid points with a spacing of $dz = 12$ km. The number of grid points on the horizontal plane, L and M, depends on the actual size of the observed sunspots (see Sect. 2). The horizontal spacing is always $dx = dy = 120$ km. A summary of these values is also included in Table 1.

We note that the inversion process performed by Firtez-DZ is done in such a way that the complexity of the atmospheric model along the vertical z-direction increases slowly. This means that the number of free parameters that are determined, at every j-step of the Stokes inversion process (i-even), also increases. More details can be found in Pastor Yabar et al. (2019, see Sect. 2.3). The number of free parameters employed in this paper is indicated in Table 2.

We slightly modified the original implementation of Firtez-DZ in order to avoid excessively modifying the temperature outside the "sensitivity region", which we denote as $[\tau_a, \tau_b]$ ($\tau_a > \tau_b$; see also Appendix A). To do so, temperature perturbations δT, calculated with the LM algorithm, are forced to exponentially decay above τ_b:

$$\delta T(z) = \delta T(z[\tau_i]) \, exp\{-2(\log \tau_b - \log \tau_i)\} \text{ if } z < z(\tau_b). \quad (4)$$

Additionally, temperature perturbations for layers below τ_a are set to be equal to those at the sensitivity region limit, namely: $\delta T(z) = \delta T(z[\tau_a])$ if $z > z(\tau_a)$.

3.2. Disambiguation module

Between the inversion of the radiative transfer equation (Sect. 3.1; i-even) and the MHS module (Sect. 3.3; i-odd), there is an intermediate step that refers to the resolution of the 180° ambiguity on the horizontal component of the magnetic field. As already mentioned in Borrero et al. (2019) (Sect. 5), the inversion of the radiative transfer equation provides the horizontal component of the magnetic field (B_x, B_y) with an ambiguity of 180° (Metcalf 1994). This means that, at every point on the solar surface (x, y), we could randomly exchange (B_x, B_y, B_z) with $(-B_x, -B_y, B_z)$ and the radiative transfer equation would yield exactly the same solution: $\mathbb{I}^{\text{syn}}(x, y, \lambda)$. If the magnetic field thus inferred is fed into the MHS module (Sect. 3.3), we would solve for a completely erroneous force balance as the electric currents derived from such a magnetic field, $j = (4\pi)^{-1}c\nabla \times B$, would be completely unrealistic.

Therefore, we first must ensure that the aforementioned ambiguity has been resolved. While there are many tools

available to solve this issue (Metcalf et al. 2006), we decided to employ the so-called non-potential field calculation method (NPFC) from Georgoulis (2005). Since the NPFC method works in a two-dimensional plane parallel to the solar surface (i.e., fixed z), we solved the 180° ambiguity at the height z that corresponds to the middle of the sensitivity region for the magnetic field $z = z(\overline{\tau})$, where $\overline{\tau}$ is defined in Eq. (A.2). This is where it makes the most sense to solve the 180° ambiguity as it is the region where the errors in the inference of $\boldsymbol{B}$ by Firtez-DZ are the smallest. Elsewhere, we simply extrapolated the solution from the NPFC method to all other z values.

3.3. Magneto-hydrostatic module

The MHS module receives the physical parameters from the disambiguation module. This is indicated by the green arrow in Fig. 2. The MHS module is based on the approach presented in Borrero et al. (2019). In that paper, we employed the "fishpack" library (Swarztrauber & Sweet 1975) to solve the following equation, which represents the MHS equilibrium in the solar atmosphere:

$$\nabla^2 P_{\mathrm{g}} = -g \frac{\partial \rho}{\partial z} + \frac{1}{c} \nabla \cdot (\boldsymbol{j} \times \boldsymbol{B}) \ . \tag{5}$$

In this paper, we employed the magnetic field inferred from the inversion of the radiative transfer equation. This is not necessarily consistent with the MHD equations and contains measurement errors (see e.g., Wiegelmann & Inhester 2010). Therefore, we solved a modified version of Eq. (5), namely

$$\nabla^2(\ln P_{\mathrm{g}}) = -\frac{gu}{K_{\mathrm{b}}} \frac{\partial}{\partial z}\left(\frac{\mu}{T}\right) - \frac{f(\beta)}{cP_{\mathrm{g}}}\left[\frac{4\pi\|\boldsymbol{j}\|^2}{c} + (\boldsymbol{j} \times \boldsymbol{B}) \cdot \boldsymbol{\nabla}(\ln P_{\mathrm{g}})\right]. \tag{6}$$

The derivation of this equation is detailed in Appendix B. Here we only need to mention that the factor $f(\beta)$ is a function that aims at limiting the effect of the Lorentz force in those regions of the solar atmosphere where the plasma-β, defined as $\beta = 8\pi P_{\mathrm{g}}/\|\boldsymbol{B}\|^2$, drops below a certain value β^*. We prescribe $f(\beta)$ as:

$$f(\beta) = \begin{cases} (\beta/\beta^*)^2 & \text{if } \beta \le \beta^* \\ 1 & \text{if } \beta > \beta^* \end{cases}, \tag{7}$$

where we adopt $\beta^* = 0.5$. Using a first estimation of the gas pressure P_{g}^{i0} (i-odd), we can solve for the left-hand side of Eq. (6) as a Poisson-like equation and obtain a new gas pressure, P_{g}^{i1}, which is then inserted back into the right-hand side, and the process continues until convergence. Each time a new gas pressure is obtained, the conversion between z and the optical depth τ_{c} changes even if the temperature is kept constant (see Appendix A and Eq. (A.1)). Convergence is assessed by requiring that the Wilson depression $z_w = z(\tau_{\mathrm{c}} = 1)$ does not vary, on average over the observed region, by more than half a vertical grid point ($\mathrm{d}z/2$) between two consecutive iterations. To this end, we defined the following χ^2-merit for the Wilson depression:

$$\chi^2(z_w^{ij+1}, z_w^{ij}) = \frac{1}{LM\mathrm{d}z^2} \sum_{l=1}^{L} \sum_{m=1}^{M} [z^{ij+1}(x_l, y_m, \tau_{\mathrm{c}} = 1) \\ - z^{ij}(x_l, y_m, \tau_{\mathrm{c}} = 1)]^2 \quad \text{with } i - \text{odd.} \tag{8}$$

With the previous conditions, convergence is achieved whenever $\chi^2(z_w^{ij+1}, z_w^{ij}) < 1/4$. The iterations performed by the MHS module are illustrated in Fig. 2 in blue boxes. We will now

assume that convergence occurs after $j = q$ iterations, resulting in a gas pressure P_{g}^{iq} with i-odd. The resulting physical parameters $[C_{\dagger}^{iq}, P_{\mathrm{g}}^{iq}, \rho^{iq}]$ are then sent back into the Stokes inversion module by Firtez-DZ (Sect. 3.1). We then increase the i-index by one, which thus becomes an even number, and again we reset the j-index to zero. This is indicated by the blue arrow in Fig. 2.

It is important to note here that the physical parameters $C_{\dagger}$ that the MHS module sends back to the Firtez-DZ inversion code (blue arrow in Fig. 2) are not exactly the same as the physical parameters C that the MHS module receives from Firtez-DZ (green arrow in Fig. 2). This occurs because even though C and $C_{\dagger}$ are the same in the (x, y, z) domain, they might differ significantly in the $(x, y, \tau_{\mathrm{c}})$ scale as the conversion between z and τ_{c} is strongly dependent on the gas pressure and density (see Eq. (A.1)).

Finally, it must be borne in mind that, in order to solve Eq. (6), we need to establish a number of boundary conditions for the gas pressure P_{g} on the left-hand side of this equation, as well as for the magnetic field and temperature on the right-hand side. The boundary conditions employed in this work are detailed in Appendix C.

3.4. Iterating between Firtez-DZ and the MHS module

As mentioned in Sect. 3.1, the inversion code Firtez-DZ iteratively determines (i-even; see red boxes in Fig. 2) the temperature, T, the vertical component of the velocity, v_z, and three components of the magnetic field, B_x, B_y, and B_z, in the three-dimensional (x, y, z) domain. These physical parameters were referred to as C. The gas pressure P_{g} was initially ($i = 0$) determined under hydrostatic equilibrium (Eq. (2)), while the density, ρ, is determined by applying the equation of state (Eq. (1)). All these parameters (C, P_{g}, and ρ) are then passed through the disambiguation module and onto the MHS module so as to determine a more consistent gas pressure through the iterative solution of Eq. (6) (i-odd; see blue boxes in Fig. 2).

At this point, at $i = 0$, or in other words before the MHS module has been applied even once, we calculate the gas pressure and density through hydrostatic equilibrium (Eq. (2)). Because ρ depends on the temperature through Eq. (1), we need to reevaluate Eq. (2) at every step of the j-index iteration (Firtez-DZ). That is why in Fig. 2, after the temperature is modified, $T^{0\,j+1} = T^{0j} + \delta T^{0j}$, we go back to Eq. (2) (see solid red arrow). However, after the application of the MHS module ($i \ge 1$), the physical parameters are directly employed to solve the radiative transfer equation inside Firtez-DZ (blue arrow in Fig. 2). In fact, for $i \ge 1$, the gas pressure is never modified by Firtez-DZ and is kept to whatever values came from the MHS module (dashed red arrow in Fig. 2; see also Sect. 3.1). The density, however, does change inside Firtez-DZ because the temperature is being changed by the LM and SVD algorithms (LM+SVD box in Fig. 2).

Finally, we note that, as mentioned in Sect. 3.3, the physical parameters $C_{\dagger}^{ij}(z)$ that come out of the MHS module and are fed back into the Firtez-DZ are in general different from those inferred from the inversion code. Consequently, the output physical parameters from the MHS module, C^{iq} (i-odd), will not necessarily produce the same $\mathbb{I}^{\mathrm{syn}}$ as the output physical parameters C^{ip} (i-even) from Firtez-DZ. As indicated by the green if-statements in Fig. 2, Firtez-DZ verifies this by measuring whether the physical parameters from the MHS module, C^{iq}, can still produce a good fit to $\mathbb{I}^{\mathrm{obs}}$. If they cannot, Firtez-DZ resumes the inversion while keeping the gas pressure fixed at
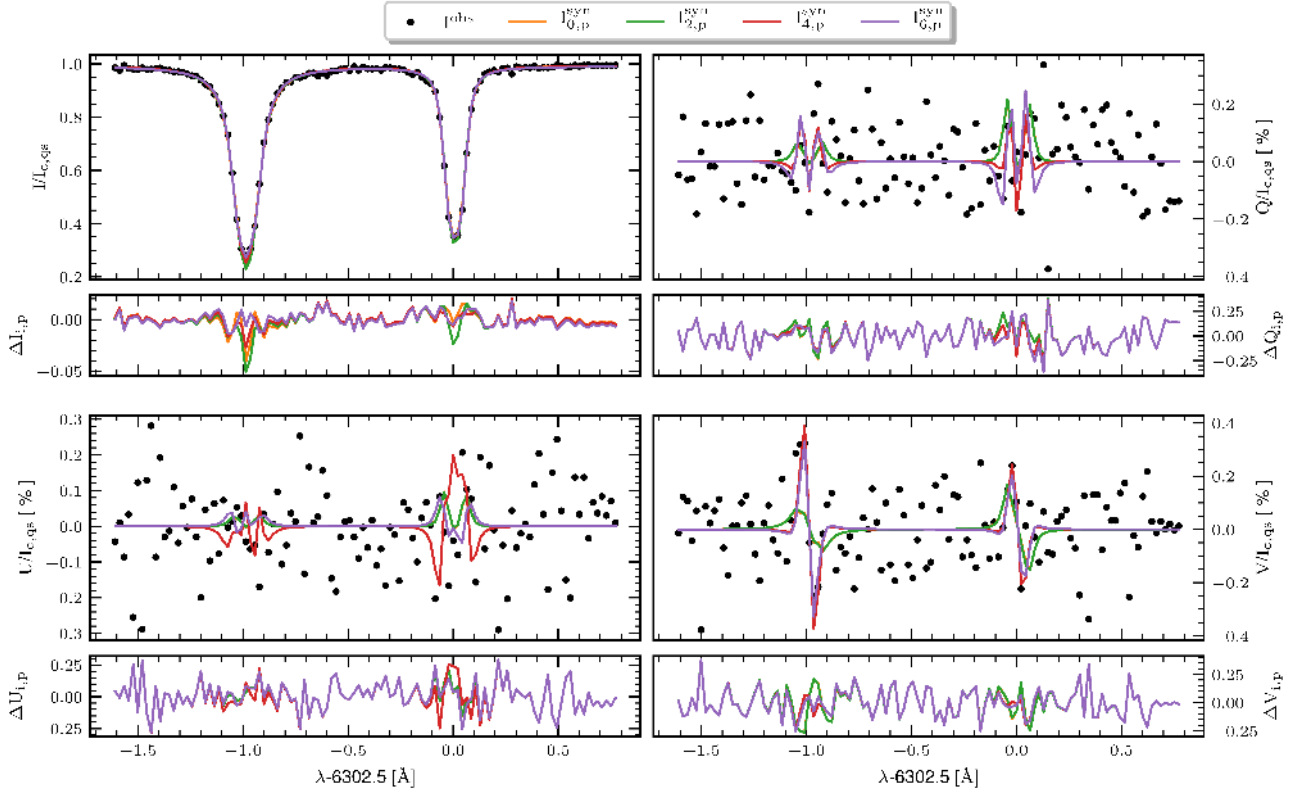
Fig. 3. Observed (black dots) and best-fit Stokes profiles (solid lines) after the application of the Firtez-DZ inversion code (*i*-even): $i = 0$ (orange), $i = 2$ (green), $i = 4$ (red), and $i = 6$ (purple). The spatial location of these profiles corresponds to a quiet-Sun pixel (red diamond in the right-hand panel of Fig. 1.) The intensity as a function of wavelength $I(\lambda)$, normalized to the average quiet-Sun continuum intensity $I_{c,qs}$, in the two Fe I lines at 630 nm is presented in the *upper-left panel*. The linear polarization profiles, $Q(\lambda)$ and $U(\lambda)$, are displayed in the *upper-right* and *lower-left panels*, respectively. Finally, the circular polarization profile, $V(\lambda)$, is shown in the *lower-right panel*.
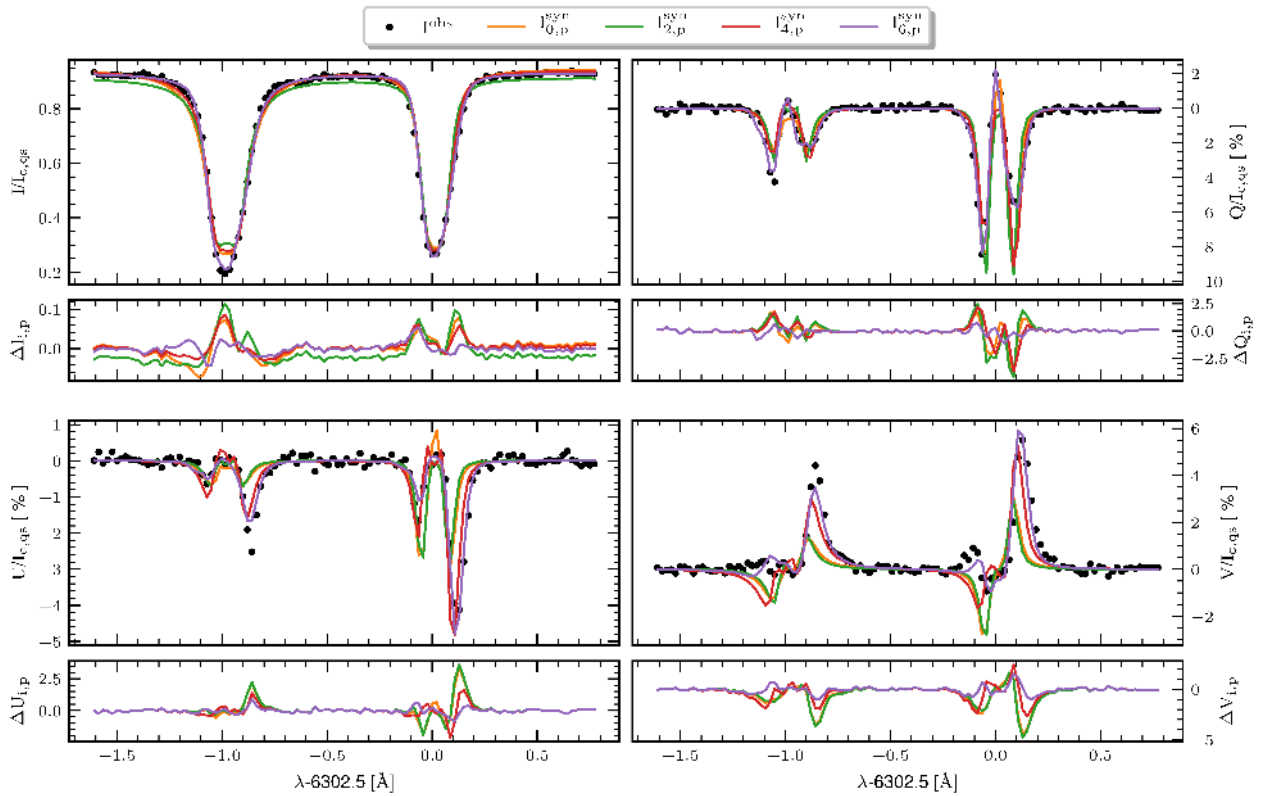
Fig. 4. Same as Fig. 3 but for a pixel located in the penumbra (see the red triangle in the right-hand panel of Fig. 1).
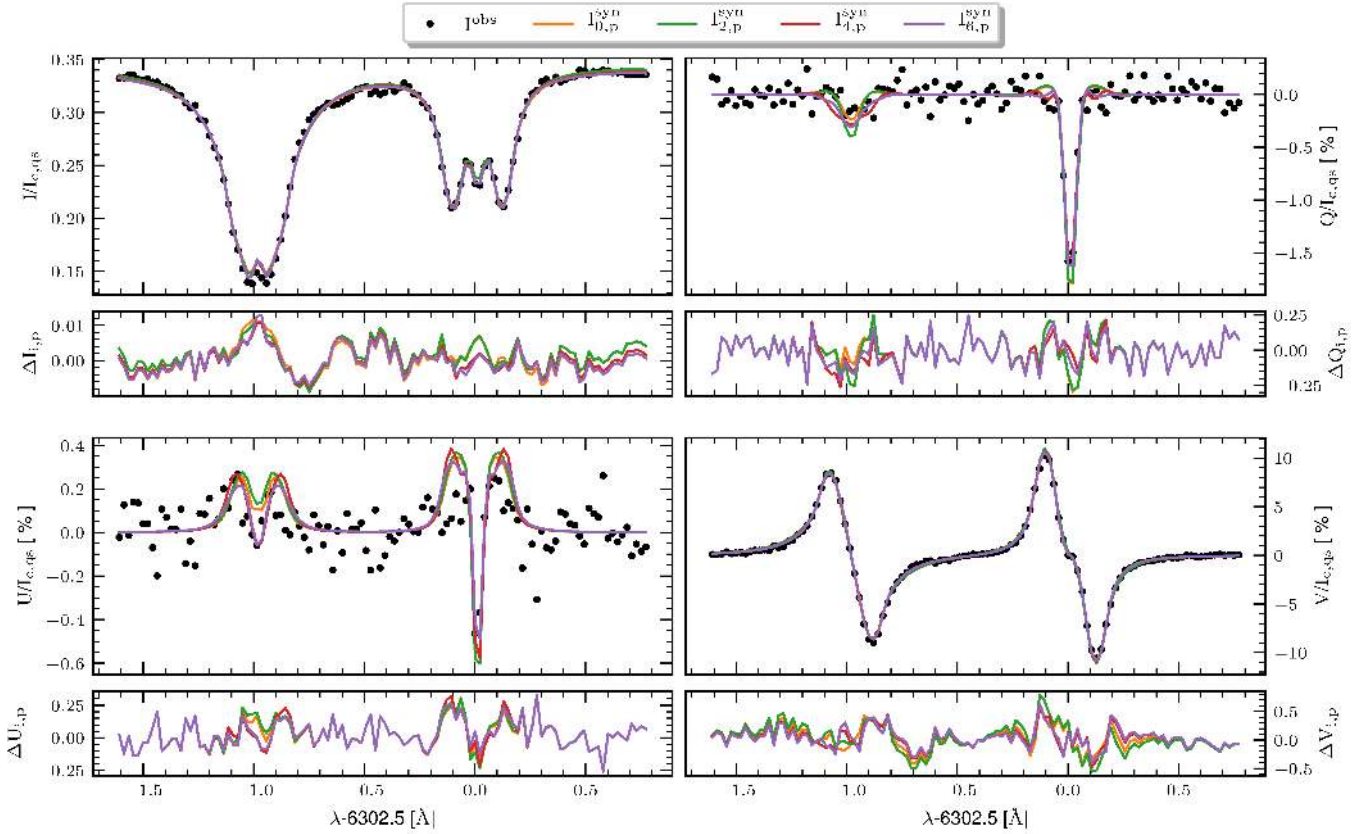
Fig. 5. Same as Fig. 3 but for a pixel located in the umbra (see the red square in the right-hand panel of Fig. 1).

P_g^{iq} (i-odd). On the other hand, if C^{iq} does indeed produce a good fit to $\mathbb{I}^{obs}$, we can consider that we have achieved convergence in both Firtez-DZ and the MHS module, and we therefore exit the process.

4. Fits to observed data

As mentioned in Sect. 1, one of the limitations in PUS2010 was that the resulting synthetic Stokes profiles, $\mathbb{I}^{syn}(x, y, \lambda)$, did not provide the best possible fit to the observed ones, $\mathbb{I}^{obs}(x, y, \lambda)$. This was more a matter of choice rather than a real limitation. The optimization process in PUS2010, based on a genetic algorithm, was too time-consuming to allow for further iterations in the inversion process. Aside from this, there was nothing preventing those authors from feeding their results in the z-scale back into the Stokes inversion code in order to continue the χ^2-minimization (Eq. (3)). This is explicitly taken into account in our method, as already explained in Sect. 3.4 and illustrated in Fig. 2. Therefore, our method can be considered as having a similar motivation as those from Riethmüller et al. (2017) and Löptien et al. (2018), in the sense that we aim at providing the best possible fit to the observed Stokes profiles. This is in contrast with PUS2010 and Asensio Ramos & Díaz Baso (2019), where fitting the observations plays a secondary role.

To showcase the quality of the fits, we present, in Figs. 3–5, three examples – in the umbra, penumbra, and quiet Sun, respectively – of the observed Stokes profiles (black dots) and the best-fit profiles (solid colored lines) after $i = 0$ (orange), $i = 2$ (green), $i = 4$ (red), and $i = 6$ (purple). These examples provide only a qualitative idea about the quality of the fits. A more quantitative picture can be drawn from Fig. 6, where we present the mean
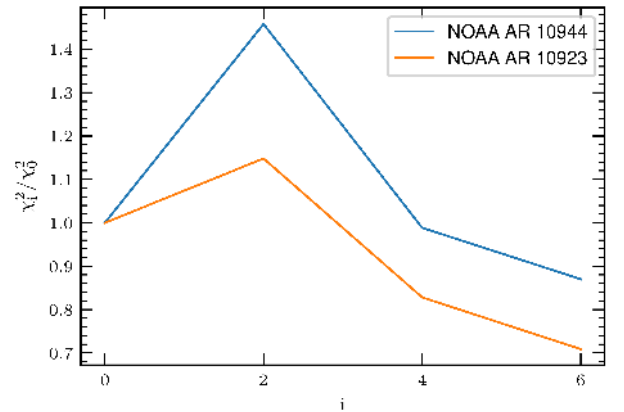
Fig. 6. Mean value of the χ^2-merit function between the observed $\mathbb{I}^{obs}(x, y, \lambda)$ and synthetic $\mathbb{I}^{syn}(x, y, \lambda)$ Stokes profiles (Eq. (3)) over the entire field-of-view as a function of the inversion iteration (i-even) performed with the Firtez inversion code (Sect. 3.1). Results for NOAA AR 10944 (left-hand panel in Fig. 1) are indicated in orange, while results for NOAA AR 10944 (right-hand panel in Fig. 1) are shown in blue.

value of $\chi^2(\mathbb{I}_{ij}^{syn}, \mathbb{I}^{obs})$ over the entire field-of-view for NOAA AR 10944 (blue; right-hand panel in Fig. 1) and NOAA AR 10923 (orange; left-hand panel in Fig. 1). As can be seen, $i = 6$ yields the best fits of the observed profiles. We note that this is simply a side effect of having the largest number of free parameters (see Table 2). This case allows us to fit even well-known asymmetric Stokes V profiles found in the sunspot penumbra, as seen in Fig. 4 (see also Sanchez Almeida & Lites 1992; Borrero et al. 2006). The important thing to consider here is not that the fit
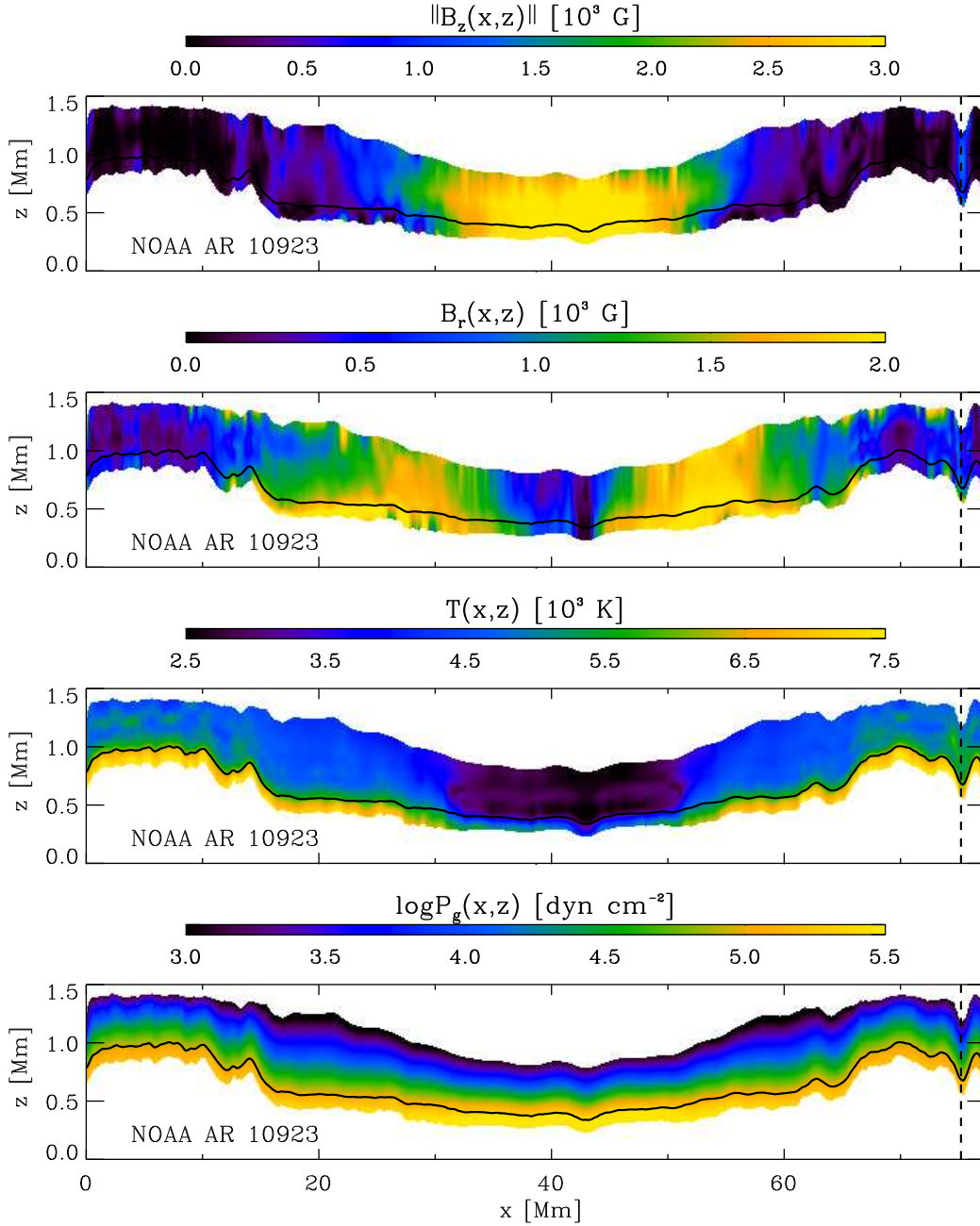
Fig. 7. Physical parameters for the sunspot NOAA AR 10923 on a vertical slice (XZ-plane) along the blue line in Fig. 1 (left-hand panel). *From top to bottom*: vertical component of the magnetic field B_z, radial component of the magnetic field B_r, temperature T, and logarithm of the gas pressure P_g. The solid black line indicates the location of the Wilson depression ($z(\tau_c = 1)$ level). See the text for more details.

improves for larger i values, but rather that it does not get worse. The reason is that the pressure and density, and hence also the optical-depth scale, are modified after each application of the MHS module (i-odd; see Sect. 3.3), thus potentially changing the synthetic profiles $\mathbb{I}^{syn}(x, y, \lambda)$ in a way that they no longer provide the best fit to the observed Stokes vector $\mathbb{I}^{obs}(x, y, \lambda)$ (see e.g., Fig. 9 in PUS2010).

5. Inferred physical parameters

Next we look at the physical parameters inferred from the combined application of the Firtez-DZ inversion code (Sect. 3.1) and the MHS constraints (Sect. 3.3). While the physical parameters are retrieved in the (x, y, z) domain, we will not consider those

regions outside $[z(\tau_a), z(\tau_b)]$, where $\tau_a = 10$ and $\tau_b = 10^{-4}$. As such, we avoid presenting results in atmospheric layers where the errors are large. As explained in Appendix A, the locations of $z(\tau_a)$ and $z(\tau_b)$ depend on the point of the solar surface (x, y) where we look. This can be illustrated by plotting the physical parameters in the XZ plane for a fixed value of y (see horizontal blue lines in Fig. 1). These physical parameters are presented in Figs. 7 and 8 for NOAA AR 10923 and 10944, respectively. In these figures, we present the absolute value of the vertical component of the magnetic field $\|B_z(x, z)\|$ (first panel), the radial component of the magnetic field $B_r(x, z) = [B_x^2(x, z) + B_y^2(x, z)]^{1/2}$ (second panel), the temperature $T(x, z)$ (third panel), and the logarithm of the gas pressure $\log P_g(x, z)$ (fourth panel). We note that NOAA AR 10923 is a negative polarity sunspot ($B_z < 0$
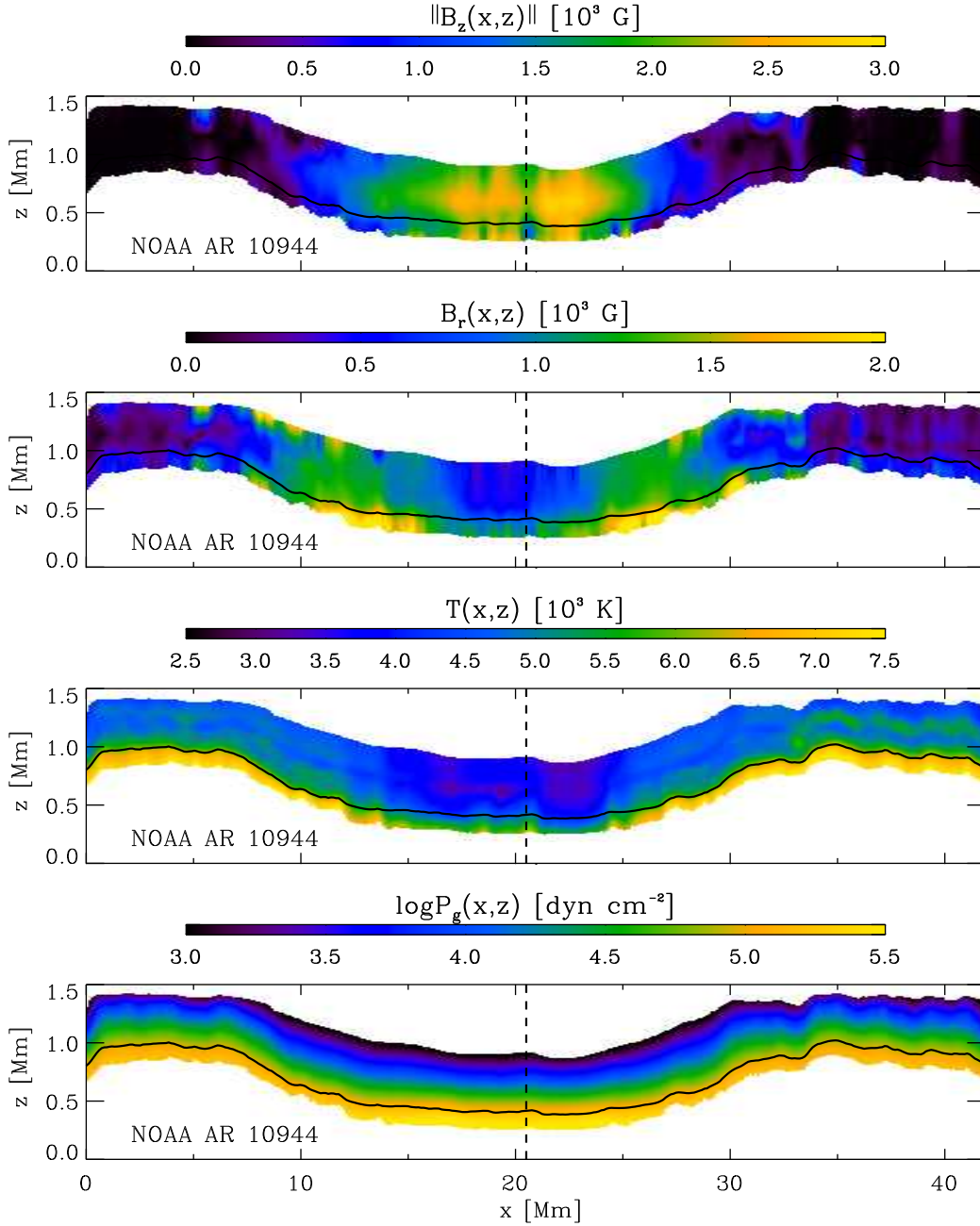
Fig. 8. Same as Fig. 7 but for the sunspot NOAA AR 10944 (right-hand panel in Fig. 1).

in the umbra) but that this is not seen because we plot only $\|B_z(x,z)\|$. Another important point is that the vertical z-scale and horizontal x-scale are not identical in these figures. While the total vertical extension of the box is about 1.5 Mm, it horizontally covers 40–60 Mm (see Sect. 3 and Table 1). Therefore, for a better visualization, we have stretched the vertical z-scale.

In Figs. 7 and 8, the solid black lines indicate the location of $z(\tau_c = 1)$ (i.e., the Wilson depression). In these figures, we can see that, along the selected slice of constant y (blue lines in Fig. 1), the location of $z(\tau_c = 1)$ is about $z \approx 1.0$ Mm in the quiet Sun, whereas in the umbra it decreases to about $z \approx 0.4-0.5$ Mm, yielding a Wilson depression of some 500–600 km. We can also notice many small-scale features. Two examples of such features are umbral dots and/or light bridges (vertical dashed line in Fig. 8 at $x \approx 21$ Mm), where we see a local enhancement in the temperature T and a local decrease in B_z at around $z \approx 0.5$ Mm. This is

accompanied by a small increase in the location of the $z(\tau_c = 1)$ level. Other interesting features are the magnetic field concentrations and magnetic knots outside the sunspot. They are seen, for instance, at $x \approx 75$ Mm in Fig. 7 (see the vertical dashed lines). These magnetic knots are characterized by having strong vertical magnetic fields of the same or opposite polarity of the sunspot's magnetic field, and they feature a strong dip at the $z(\tau_c = 1)$ level.

In Figs. 9 and 10, we show the two-dimensional (x, y) maps of the geometrical height at which different τ_c levels are reached in NOAA AR 10923 and 10944, respectively. All values are given with respect to the quiet Sun $z_{qs}(\tau_c)$ (see white rectangles in these figures). These maps correspond to four different realizations of the $z - \tau_c$ conversion (see Eq. (A.1)) over the entire observed regions. Again, our method is capable of inferring the small-scale structure of the conversion between

$$z_{qs}(\tau_c) - z(x, y, \tau_c)$$
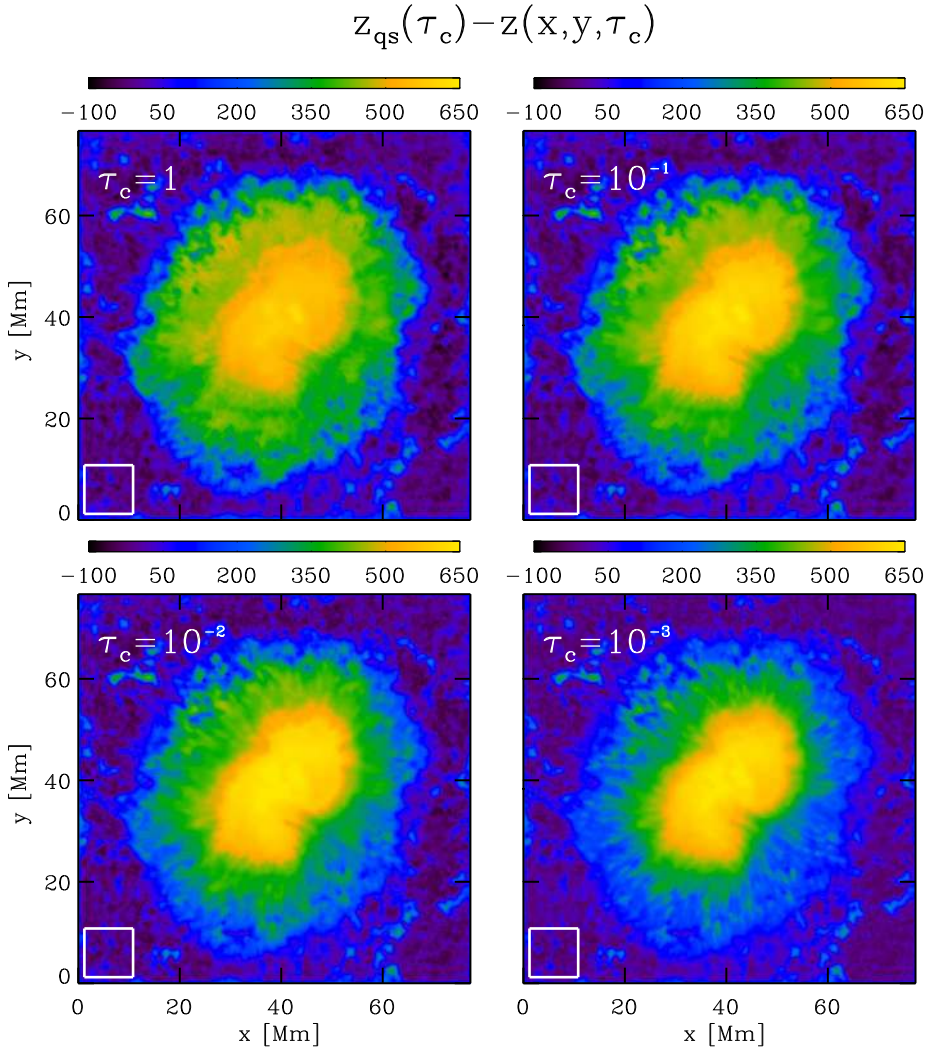
Fig. 9. Maps of the geometrical height at which different τ_c levels are reached in NOAA AR 10923: $\tau_c = 1$ (*top left*), $\tau_c = 10^{-1}$ (*top right*), $\tau_c = 10^{-2}$ (*bottom left*), and $\tau_c = 10^{-3}$ (*bottom right*). All values are given with respect to the geometrical height for that τ_c level in the quiet Sun, $z_{qs}(\tau_c)$. The quiet-Sun value is calculated as the spatial average over the white rectangle.

geometrical height z and optical depth τ_c. This is clearly seen around the light bridges in both sunspots as well as the magnetic knots around them. The mean values of the Wilson depression, $z_{qs}(\tau_c = 1) - z(\tau_c = 1)$, in the umbra obtained with our method are 588 km for NOAA AR 10923 (Fig. 9; upper-left panel) and 524 km for NOAA A 10944 (Fig. 10; upper-left panel). The maximum values around are 630 and 580 km, respectively.

It is important to notice that panels for each τ_c level differ. This is a consequence of our method being capable of stretching and/or shrinking the $z - \tau$ scale between consecutive grid points along the vertical direction through the changes in temperature, density, and pressure (see Eq. (A.1)). Other methods, where the $z - \tau$ conversion is obtained by simply shifting, at each (x, y)-location, the entire z-scale up or down, would yield exactly the same results at different τ_c levels in Figs. 9 and 10.

6. Conclusions

We have presented a new inversion code for the polarized radiative transfer equation that is capable of retrieving the physical parameters in the solar photosphere in the (x, y, z) domain in a way that is consistent with the MHS equations, and therefore it takes into account the effects of the Lorentz force (magnetic tension and pressure) in the force balance. Because of this, our new inversion code is capable of inferring not only the three components of the magnetic field, the temperature, and the line-of-sight

velocity, but also the gas pressure and density in the solar photosphere. The development of this code is inspired, albeit loosely, on the work by Puschmann et al. (2010).

The inversion code makes use of the Firtez-DZ code and an MHS solver that have been described and tested separately by Pastor Yabar et al. (2019) and Borrero et al. (2019), respectively, employing results from three-dimensional MHD simulations of sunspots (Rempel 2012). In this paper, we combine both approaches into a single one and test its results with spectropolarimetric observations from the Hinode/SP instrument in two sunspots located very close to disk center.

To put our new approach in context, we will categorize all available methods (Carroll & Kopf 2008; Puschmann et al. 2010; Riethmüller et al. 2017; Löptien et al. 2018; Asensio Ramos & Díaz Baso 2019) that also aim at retrieving the physical parameters in the (x, y, z) domain into those that: (a) can be applied to large regions of the solar surface (i.e., entire sunspots plus their surrounding plage, moat, and quiet Sun); (b) infer the small-scale structure (i.e., umbral dots, penumbral filaments, light bridges, magnetic knots, etc.); and (c) fit the observed Stokes vector. All of the aforementioned methods give priority to some features at the expense of others. For instance, Löptien et al. (2018) limit the number of Fourier coefficients in order to analyze large fields-of-view, thereby limiting their ability to retrieve small-scale structures. Puschmann et al. (2010) make the opposite sacrifice. The Asensio Ramos & Díaz Baso (2019) method can deal with both

$$z_{qs}(\tau_c) - z(x, y, \tau_c)$$
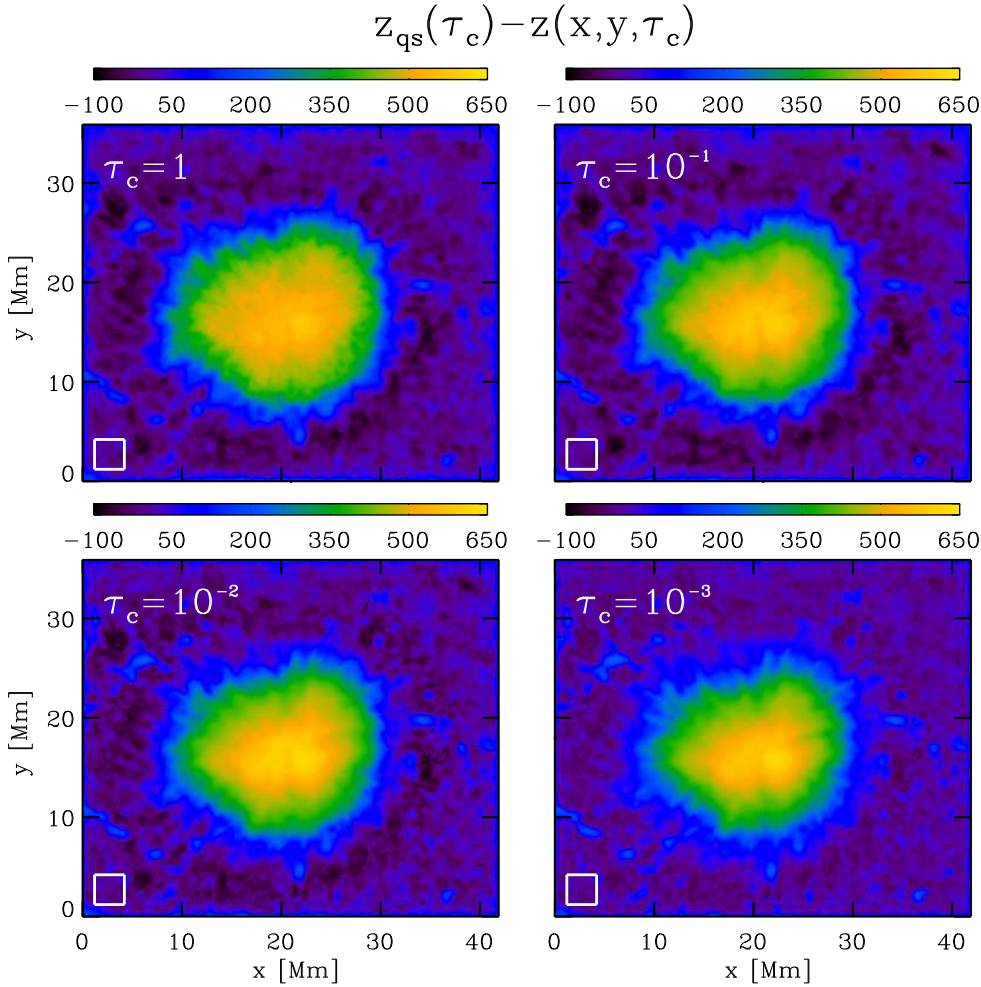
Fig. 10. Same as Fig. 9 but for NOAA AR 10944.

situations but does not provide the best possible fit to the observed Stokes vector. Although our method meets the three previous requirements, there is a very obvious drawback: its speed. Just to give some numbers: the first iteration cycle ($i = 0$) took totals of 500 (small spot) or 2000 (large spot) combined CPU (central processing unit) hours. Later iterations ($i \geq 2$) needed about half this. Although the actual running time was significantly reduced by running our inversions in clusters with several hundred nodes, our method is not yet suitable for processing large amounts of data. Therefore, which of the available methods is to be preferred depends on the particular use case.

Our inversion code also yields, in a natural way, the Wilson depression across the solar surface, not only at $\tau_c = 1$ but at all optical depths within the region where the analyzed spectral lines are formed. Our values for the inferred Wilson depression are compatible, albeit somewhat smaller, by about 50–70 km, with similar studies of the same sunspots (Löptien et al. 2018, 2020; Asensio Ramos & Díaz Baso 2019). We note, however, that those studies were carried out with inversion results that considered the effects of the telescope and instrument point spread function (PSF). Those inversions usually retrieve sharper variations of the magnetic field along the (x, y)-directions, which is likely the reason our results differ from theirs. We will study this particular point in more detail in a future work by implementing the coupled-inversion technique by van Noort (2012) into our code, in order to remove the smearing effects introduced by the instrumental PSF.

It is also desirable to check how close to solenoidal the inferred magnetic field $\boldsymbol{B}(x, y, z)$ is. This might imply the implementation of a new approach, within our inversion code, to minimize $\boldsymbol{\nabla} \cdot \boldsymbol{B}$. Therefore, we have decided to leave it for a future study. Such minimization seems to help improve the results of the inferences in the (x, y, z) domain (Puschmann et al. 2010; Löptien et al. 2018). We are not sure, however, how much our method will benefit from such an implementation as methods that minimize $\boldsymbol{\nabla} \cdot \boldsymbol{B}$ typically only modify the potential component of the magnetic field while leaving the non-potential component, and hence the electric currents $\boldsymbol{j} \propto \boldsymbol{\nabla} \times \boldsymbol{B}$, untouched (Tóth 2000). Consequently, none of those methods would have any effect on the MHS force balance as implemented in our code (Eq. (6); Appendix B).

A corollary of the discussion in the previous paragraph is that, in its current state, our inversion code can be used to infer realistic electric currents $\boldsymbol{j}$ even if the magnetic field is not close to being solenoidal. We foresee future applications where the full $\boldsymbol{j}$-vector, instead of simply its vertical j_z-component, is employed to study the evolution of magnetic structures on the solar surface that are likely to produce enhanced chromospheric and coronal activity (see e.g., Solanki et al. 2003; Wang et al. 2017).

References

Asensio Ramos, A., & Díaz Baso, C. J. 2019, A&A, 626, A102
Asensio Ramos, A., Requerey, I. S., & Vitas, N. 2017, A&A, 604, A11
Bellot Rubio, L. R. 2006, in Solar Polarization 4, eds. R. Casini, & B. W. Lites, ASP Conf. Ser., 358, 107
Borrero, J. M., Solanki, S. K., Lagg, A., Socas-Navarro, H., & Lites, B. 2006, A&A, 450, 383
Borrero, J. M., Lites, B. W., Lagg, A., Rezaei, R., & Rempel, M. 2014, A&A, 572, A54
Borrero, J. M., Pastor Yabar, A., Rempel, M., & Ruiz Cobo, B. 2019, A&A, 632, A111
Carroll, T. A., & Kopf, M. 2008, A&A, 481, L37
del Toro Iniesta, J. C. 2003a, Astron. Nachr., 324, 383
del Toro Iniesta, J. C. 2003b, Introduction to Spectropolarimetry (Cambridge, UK: Cambridge University Press)
del Toro Iniesta, J. C., & Ruiz Cobo, B. 2016, Liv. Rev. Sol. Phys., 13, 4
Georgoulis, M. K. 2005, ApJ, 629, L69
Golub, G., & Kahan, W. 1965, SIAM J. Numer. Anal., 2, 205
Ichimoto, K., Suematsu, Y., & Shimizu, T. 2007, in New Solar Physics with Solar-B Mission, eds. K. Shibata, S. Nagata, & T. Sakurai, ASP Conf. Ser., 369, 39
Jurčák, J., Collados, M., Leenaarts, J., van Noort, M., & Schlichenmaier, R. 2019, Adv. Space Res., 63, 1389
Kippenhahn, R., & Moellenhoff, C. 1975, Mannheim West Germany Bibliographisches Institut AG
Kosugi, T., Matsuzaki, K., Sakao, T., et al. 2007, Sol. Phys., 243, 3
Landi Degl'Innocenti, E., & Landi Degl'Innocenti, M. 1985, Sol. Phys., 97, 239
Lites, B. W., Elmore, D. F., & Streander, K. V. 2001, in Advanced Solar Polarimetry - Theory, Observation, and Instrumentation, ed. M. Sigwarth, ASP Conf. Ser., 236, 33
Löptien, B., Lagg, A., van Noort, M., & Solanki, S. K. 2018, A&A, 619, A42
Löptien, B., Lagg, A., van Noort, M., & Solanki, S. K. 2020, A&A, 635, A202
Maltby, P. 1977, Sol. Phys., 55, 335
Martinez Pillet, V., & Vazquez, M. 1990, Ap&SS, 170, 75
Martinez Pillet, V., & Vazquez, M. 1993, A&A, 270, 494
Mathew, S. K., Solanki, S. K., Lagg, A., et al. 2004, A&A, 422, 693
Metcalf, T. R. 1994, Sol. Phys., 155, 235
Metcalf, T. R., Leka, K. D., Barnes, G., et al. 2006, Sol. Phys., 237, 267
Mihalas, D. 1970, Stellar Atmospheres (San Francisco: Freeman)
Pastor Yabar, A., Borrero, J. M., & Ruiz Cobo, B. 2019, A&A, 629, A24
Press, W. H., Flannery, B. P., & Teukolsky, S. A. 1986, Numerical Recipes. The Art of Scientific Computing (Cambridge: Cambridge University Press)
Priest, E. R. 1984, Solar Magneto-hydrodynamics
Puschmann, K. G., Ruiz Cobo, B., & Martínez Pillet, V. 2010, ApJ, 720, 1417
Rempel, M. 2012, ApJ, 750, 62
Riethmüller, T. L., Solanki, S. K., Barthol, P., et al. 2017, ApJS, 229, 16
Rimmele, T. R., Warner, M., Keil, S. L., et al. 2020, Sol. Phys., 295, 172
Ruiz Cobo, B. 2007, in Modern Solar Facilities - Advanced Solar Science, eds. F. Kneer, K. G. Puschmann, & A. D. Wittmann, 287
Ruiz Cobo, B., & del Toro Iniesta, J. C. 1994, A&A, 283, 129
Sanchez Almeida, J., & Lites, B. W. 1992, ApJ, 398, 359
Schlichenmaier, R., Rezaei, R., Bello González, N., & Waldmann, T. A. 2010, A&A, 512, L1
Schlichenmaier, R., von der Lühe, O., Hoch, S., et al. 2016, A&A, 596, A7
Shimizu, T., Nagata, S., Tsuneta, S., et al. 2008, Sol. Phys., 249, 221
Socas-Navarro, H. 2001, in Advanced Solar Polarimetry - Theory, Observation, and Instrumentation, ASP Conf. Ser., 236, 487
Solanki, S. K., Walther, U., & Livingston, W. 1993, in IAU Colloq. 141: The Magnetic and Velocity Fields of Solar Active Regions, eds. H. Zirin, G. Ai, & H. Wang, ASP Conf. Ser., 46, 48
Solanki, S. K., Lagg, A., Woch, J., Krupp, N., & Collados, M. 2003, Nature, 425, 692
Suematsu, Y., Tsuneta, S., Ichimoto, K., et al. 2008, Sol. Phys., 249, 197
Swarztrauber, P., & Sweet, R. 1975, Efficient FORTRAN Subprograms for the Solution of Elliptic Partial Differential Equations
Tóth, G. 2000, J. Comput. Phys., 161, 605
Tsuneta, S., Ichimoto, K., Katsukawa, Y., et al. 2008, Sol. Phys., 249, 167
van Noort, M. 2012, A&A, 548, A5
Wang, H., Liu, C., Ahn, K., et al. 2017, Nat. Astron., 1, 0085
Wiegelmann, T., & Inhester, B. 2010, A&A, 516, A107

Appendix A: $z - \tau_c$ conversion and sensitivity regions

The conversion between the continuum optical depths τ_c and z depends on the density and continuum opacity κ_c, which in turn depends on the gas pressure and temperature, as:

$$d\tau_c = -\rho\kappa_c(P_g, T)dz . \tag{A.1}$$

Let us define $z_a = z(\tau_a)$ and $z_b = z(\tau_b)$ as the locations of the optical depths τ_a and τ_b that cover the sensitivity region of the spectral lines to the physical parameters C as determined by Firtez-DZ. We note that $\tau_a > \tau_b$, whereas $z_a < z_b$ because the optical-depth scale and the geometrical scale grow in opposite directions (see Eq. (A.1)). It is important to bear in mind that, due to its dependence on the density and opacity, Eq. (A.1) implies that the locations z_a and z_b are different for every (x, y) position.

Owing to the fact that different spectral lines are sensitive to different regions in the solar atmosphere (Ruiz Cobo & del Toro Iniesta 1994), we adopted $[\tau_a, \tau_b] = [10, 10^{-4}]$ in this work. With this, we can define the optical depth location that corresponds to the "middle" of the sensitivity region as:

$$\widetilde{\tau} = 10^{\frac{1}{2}[\log \tau_a + \log \tau_b]} . \tag{A.2}$$

This yields $\widetilde{\tau} \approx 0.0316$. The values of τ_a, τ_b, and $\widetilde{\tau}$ depend, of course, on the observed spectral lines (see Sect. 2). The more spectral lines that are observed, the larger the sensitivity region becomes.

Appendix B: MHS equation

Let us start with the momentum equation in ideal MHS (see Eq. 16.23 in Kippenhahn & Moellenhoff 1975):

$$\nabla P_g = \rho g + c^{-1} j \times B , \tag{B.1}$$

where P_g, ρ, and $g = -ge_z$ stand for the gas pressure, density, and the Sun's gravity acceleration, respectively. These were introduced in Sect. 3.1. The term $c^{-1} j \times B$ corresponds to the Lorentz force and can be decomposed into the magnetic pressure and the magnetic tension (Priest 1984, Sect. 2.7; Eq. (2.56)). In Borrero et al. (2019), we took the divergence of this equation to transform it from a system of three first-order partial differential equations into a single second-order partial differential equation. Here we will proceed along those same lines, but first we will employ the equation of state (Eq. (1)) to substitute the above density, as well as divide the left-hand side and the right-hand side by the gas pressure:

$$\frac{\nabla P_g}{P_g} = \frac{u}{K_b} \frac{\mu}{T} g + \frac{1}{c} \frac{j \times B}{P_g} . \tag{B.2}$$

This equation can be further transformed as follows:

$$\nabla(\ln P_g) = -\frac{ug}{K_b} \frac{\mu}{T} e_z + \frac{1}{c} \frac{j \times B}{P_g} . \tag{B.3}$$

Finally, we take the divergence of the equation above, which yields:

$$\nabla^2(\ln P_g) = -\frac{ug}{K_b} \frac{\partial}{\partial z}\left[\frac{\mu}{T}\right] + \frac{1}{c}\nabla \cdot \left[\frac{j \times B}{P_g}\right] . \tag{B.4}$$

Unlike Eq. (5), solving Eq. (B.4) will always yield $P_g > 0$. While this was not critical when employing physical parameters resulting from MHD simulations (Borrero et al. 2019), we are now determining the right-hand side using a magnetic field (B) and temperature (T) that have been inferred from the observations via the inversion of the radiative transfer equation (Sect. 3.1). They are therefore affected by measurement errors, which become exponentially larger as we consider regions outside the sensitivity region of the spectral line (see Appendix A). Consequently, when dealing with actual observations, Eq. (B.4) is highly preferable.

We will now focus our attention on the second term on the right-hand side of Eq. (B.4) (highlighted in red) and expand the divergence operator as:

$$\nabla \cdot \left[\frac{j \times B}{P_g}\right] = \frac{1}{P_g}[\nabla \cdot (j \times B) - (j \times B) \cdot \nabla(\ln P_g)] , \tag{B.5}$$

where the first term on the right-hand side (again highlighted in red) of the above equation can be further expanded, employing basic vector identities, as:

$$\nabla \cdot (j \times B) = -\frac{c}{4\pi}[(\nabla^2 B)B + \|\nabla \times B\|^2]. \tag{B.6}$$

We can see here that the first term on the right-hand side of Eq. (B.6) involves second-order spatial derivatives of the magnetic field, whereas the second term on the right-hand side involves the square of first-order derivatives. Unlike MHD simulations, where grid sizes are typically on the order of a few kilometers, observational grid sizes are much larger (see Sect. 2 and Table 1) and therefore second-order derivatives will be much more inaccurate than first-order ones. For this reason, we decided to neglect the first term on the right-hand side of Eq. (B.6) ($\nabla^2 B$) and retain only the second term ($\|\nabla \times B\|^2$). In the future, it might be possible to include the neglected term as new observing facilities, such as the *Daniel K. Inouye* Solar Telescope (DKIST; Rimmele et al. 2020) and the European Solar Telescope (EST; Jurčák et al. 2019), will provide spectropolarimetric observations, also with a spatial resolution of a few kilometers. Once we insert the simplified Eq. (B.6) into Eq. (B.5) and into Eq. (B.4) we obtain:

$$\nabla^2(\ln P_g) = -\frac{ug}{K_b}\frac{\partial}{\partial z}\left[\frac{u}{T}\right] - \frac{1}{cP_g}\left[\frac{4\pi\|j\|^2}{c} + (j \times B) \cdot \nabla(\ln P_g)\right]. \tag{B.7}$$

Next we consider that, as we approach the highest layers of the solar photosphere (i.e., close to the temperature minimum), the density and gas pressure are so low that the Lorentz force term dominates the force balance (Eq. (B.1)). At this point, large velocities also usually appear (oftentimes supersonic and super-Alfvenic) so that the advection term ($\rho(v \cdot \nabla) \cdot v$) starts to play an important role. Unfortunately, the velocity term is not included in our force balance (Eqs. (5), (6), (B.1)) simply because we do not have access, via spectropolarimetry, to the horizontal components of the velocity. Until such time that we implement a new method to determine v_x and v_y (see e.g., Asensio Ramos et al. 2017), we will take a pragmatic approach and consider that the advection term partially compensates for the Lorentz force term as we approach regions with very low plasma-β. To mimic this effect, we introduced a scaling function $f(\beta)$ that reduces the effect of the Lorentz force in regions where $\beta \geq 0.5$ (see Eq. (7)). Our approach is justified by the fact that the advection term partially compensates for the Lorentz force term in the high photosphere in MHD simulations (Rempel 2012), bringing the force balance close to hydrostatic equilibrium.

Appendix C: Boundary conditions

In the following, we describe the boundary conditions employed to solve Eq. (6). The need for these boundary conditions was mentioned in the last paragraph of Sect. 3.3.

C.1. P_g boundary conditions: Non-axially symmetric sunspots

The boundary conditions for the gas pressure apply to the left-hand side of Eq. (6) and must be known for all six sides of the three-dimensional volume. These sides are characterized by $x_1 = y_1 = z_1 = 0$ and by $x_L = L\mathrm{d}x$, $y_M = M\mathrm{d}y$, $z_N = N\mathrm{d}z$ (see Table 1). In this paper, we consider only Dirichlet boundary conditions. In Borrero et al. (2019, see Eq. (9)), we employed axially symmetric boundary conditions for P_g. In this paper, we continue using the same values for the side boundaries: $P(x_1, y, z)$, $P(x_L, y, z)$, $P(x, y_1, z)$, and $P(x, y_M, z)$. These are adequate as long as the analyzed sunspot is fully surrounded by quiet Sun on all four sides. This is indeed our case (see Sect. 2). In the z-direction, we adopted a different approach that does not assume axial symmetry. This is important because, more often than not, sunspots have elliptical shapes, contain umbral dots or light bridges, are surrounded by plage or pores, the penumbra is unevenly developed, etc. (Schlichenmaier et al. 2010, 2016). To account for this possibility, we instead employed the following empirical boundary conditions at $z = z_1$ and $z = z_N$:

$$\log P_g^{ij}(x, y, z_1) = \quad 6.19 - 4.57 \times 10^{-5} \|B_z^{ij}(x, y, \widetilde{\tau})\|$$
$$\log P_g^{ij}(x, y, z_N) = \quad 2.44 - 9.55 \times 10^{-4} \|B_z^{ij}(x, y, \widetilde{\tau})\| , \quad (\text{C.1})$$

where $\|B_z^{ij}(x, y, \widetilde{\tau})\|$ refers to the modulus of the vertical component of the magnetic field at an optical depth corresponding to the middle of the sensitivity region $\widetilde{\tau}$ (Eq. (A.2)). To get an idea about the values that Eq. (C.1) yields, we can consider that, in the quiet Sun, $\|B_z(\widetilde{\tau})\| \approx 0$ Gauss, thus resulting in $P_g(z_1) \approx 250 \,\mathrm{dyn\,cm^{-2}}$ and $P_g(z_N) \approx 1.55 \times 10^6 \,\mathrm{dyn\,cm^{-2}}$. On the other hand, taking a value of $\|B_z(\widetilde{\tau})\| \approx 4000$ Gauss for a strong umbra, we obtain $P_g(z_1) \approx 0.04 \,\mathrm{dyn\,cm^{-2}}$ and $P_g(z_N) \approx 1.02 \times 10^6 \,\mathrm{dyn\,cm^{-2}}$. These values are in qualitative agreement with the results from three-dimensional MHD simulations of sunspots (Rempel 2012).

The purpose of these boundary conditions is to speed up the convergence of the MHS module (Sect. 3.3). Using significantly different boundary conditions results in very similar results to those presented in Sect. 5. We have tested that this is the case by running the MHS module with $P_g(z_1) = 1.25 \times 10^6 \,\mathrm{dyn\,cm^{-2}}$ and $P_g(z_N) = 2.5 \,\mathrm{dyn\,cm^{-2}}$, which are the same at every (x, y), over the lowermost $z = z_1$ and uppermost $z = z_N$ planes. These results are in agreement with Borrero et al. (2019), where the role of the boundary conditions was studied in more detail.

C.2. T and **B** outside the sensitivity regions

At the beginning of Sect. 3.1, we introduced the physical parameters $C^{ij} = [T, B_x, B_y, B_z]$. In principle, we could use the physical parameters C^{ij} inferred from the inversion to solve Eq. (6). However, the inversion retrieves very unreliable values outside the sensitivity region $[z_a, z_b]$ (see Appendix A), and therefore we will change the physical parameters outside this region to more meaningful values. This will not interfere with our ability to fit the observed Stokes vector because the spectral lines are not sensitive to whatever happens outside $[z_a, z_b]$. Consequently,

we do not directly employ C^{ij} on the right-hand side of Eq. (6) but rather $C_\dagger^{ij}$, which is constructed from the previous as follows:

$$C_\dagger^{ij}(z) = \begin{cases} C(z_1) + \frac{C^{ij}(z_a) - C(z_1)}{z_a - z_1}(z - z_1) & \text{if } z < z_a \\ C^{ij}(z) & \text{if } z \in [z_a, z_b] \\ C(z_N) + \frac{C^{ij}(z_b) - C(z_N)}{z_b - z_N}(z - z_N) & \text{if } z > z_b \end{cases} . \quad (\text{C.2})$$

Here we see that $C_\dagger = C$ inside the sensitivity region, and therefore we kept the physical parameters as determined by the Firtez-DZ inversion code (Sect. 3.1). Outside the sensitivity region, we performed a linear interpolation between z_1 and z_a as well as between z_b and z_N. Since the values at z_a and z_b are reliable and are provided by the inversion, all we need to do is establish the values at the boundaries z_1 and z_N; then, by virtue of the linear interpolation in Eq. (C.2), we can determine the physical parameters everywhere outside the sensitivity region. We note that Eq. (C.2) must be applied separately for each (x, y) grid point on the horizontal plane because z_a and z_b change horizontally (see Appendix A). Also, it is important to bear in mind that Eq. (C.2) must be applied after every j-iteration of the solution of Eq. (6) (see Sect. 3.3) as well because P_g^{ij} and ρ^{ij} change with each j-iteration and hence so do the locations where $z = z(\tau_a)$ and $z = z(\tau_b)$ (see Eq. (A.1)).

For the temperature at the uppermost boundary, we simply say that $T(z_N) = T(z_b)$, and therefore the temperature for $z > z_b$ is always constant and equals $T(z_b)$ (i.e., no interpolation needed). At the lowermost boundary, we employed a method similar to the one described in Borrero et al. (2019) (Sect. 4.2), in which we perform azimuthal averages of $T(x, y, z_1)$ as provided by the three-dimensional simulations of sunspots Rempel (2012) and fit the resulting radial dependence with a fourth-order polynomial. The resulting polynomial, as a function of the normalized radial distance $\xi = r/R$ (R is the sunspot radius), is:

$$\log T(\xi, z_1) = 3.957 + 0.024\xi + 0.439\xi^2 - 0.392\xi^3$$
$$+ 0.094\xi^4. \quad (\text{C.3})$$

Equation (C.3) yields temperatures of approximately 9000 K and 13 500 K at z_1 in the center of the umbra ($\xi = 0$) and in the quiet Sun ($\xi = 2$), respectively.

We will now focus on the horizontal components of the magnetic field. At $z = z_N$ and $z = z_{N-1}$, we consider that they vanish, whereas at $z = z_1$ we take them to be the same as those in the middle of the sensitivity region (this last condition also applies to the vertical component of the magnetic field):

$$B_x^{ij}(z_N) = B_x^{ij}(z_{N-1}) = 0$$
$$B_y^{ij}(z_N) = B_y^{ij}(z_{N-1}) = 0$$
$$B_x^{ij}(z_1) = B_x^{ij}(z[\overline{\tau}]) \quad (\text{C.4})$$
$$B_y^{ij}(z_1) = B_x^{ij}(z[\overline{\tau}])$$
$$B_z^{ij}(z_1) = B_z^{ij}(z[\overline{\tau}]).$$

The last boundary condition we need is that of the vertical component of the magnetic field at the uppermost boundary, $B_z^{ij}(z_N)$. To find it, we first write the radial component of the momentum equation in cylindrical coordinates at the uppermost z-plane, which, once we apply the boundary conditions for the B_x and B_y components of the magnetic field given by Eq. (C.4), simplifies into:

$$\frac{\partial}{\partial r}\left(P_g + \frac{B_z^2}{8\pi}\right) = 0 . \quad (\text{C.5})$$

Using this, we can readily determine the boundary condition for the vertical component of the magnetic field at $z = z_N$:

$$B_z^{ij}(x, y, z_N) = \sqrt{8\pi[P_{g,qs}^{ij}(z_N) - P_g^{ij}(x, y, z_N)]} , \qquad (C.6)$$

where the values of the gas pressure at z_N can be obtained from Eq. (C.1) by inserting the values of the z-component of the magnetic field in the middle of the sensitivity region: $B_z^{ij}(x, y, \widetilde{\tau})$. The quiet-Sun values $P_{g,qs}^{ij}$ are obtained by setting the magnetic field in Eq. (C.1) to zero.